crystals

MDPI

Article

U–Pb Dating, Gemology, and Chemical Composition of Apatite from Dara-e-Pech, Afghanistan

Biying Lai [1,2], Bo Xu [1,2,*] and Yi Zhao [1]

[1] Frontiers Science Center for Deep-Time Digital Earth and State Key Laboratory of Geological Processes and Mineral Resources, China University of Geosciences, Beijing 100083, China; 2009210028@email.cugb.edu.cn (B.L.); zhaoyi0102@cugb.edu.cn (Y.Z.)
[2] The Beijing SHRIMP Center, Chinese Academy of Geological Sciences, Beijing 100037, China
* Correspondence: bo.xu@cugb.edu.cn

Abstract: Minerals of the apatite group commonly occur in granite pegmatites, and their ability to incorporate a wide range of trace elements makes them a good indicator of magma composition and magmatic–hydrothermal processes. Gem-quality purple apatite crystals from the Dara-e-Pech pegmatite field in Afghanistan have rarely been reported. Here, we investigated apatite crystals originated from this locality, using gemological testing, chemical analysis, and in situ U–Pb dating, with the purpose of identifying their origin, the constraints on the magma source in which the apatite crystals were formed, and the timing of the magmatic–hydrothermal activity. Our findings demonstrate that the purple apatite crystals were impure fluorapatite, characterized by heavy rare-earth element (HREE) enrichment, intermediate Eu anomalies, and non-CHARAC Y/Ho ratios. The results showed that these apatite crystals yielded a lower intercept age of 135.8 ± 6.9 Ma. We proposed that the pegmatitic apatite samples formed in a transitional magmatic–hydrothermal pegmatitic system with moderate fO_2 in the Early Cretaceous (~135 Ma). Our study helps to constrain the magmatic–hydrothermal activities of the little-known Dara-e-Pech pegmatite field.

Keywords: apatite; gemological characteristic; chemical composition; U–Pb dating; Dara-e-Pech

check for updates

Citation: Lai, B.; Xu, B.; Zhao, Y. U–Pb Dating, Gemology, and Chemical Composition of Apatite from Dara-e-Pech, Afghanistan. *Crystals* **2024**, *14*, 34. https://doi.org/10.3390/cryst14010034

Academic Editor: Vladislav V. Gurzhiy

Received: 8 November 2023
Revised: 28 November 2023
Accepted: 4 December 2023
Published: 27 December 2023

Copyright: © 2023 by the authors. Licensee MDPI, Basel, Switzerland. This article is an open access article distributed under the terms and conditions of the Creative Commons Attribution (CC BY) license (https://creativecommons.org/licenses/by/4.0/).

1. Introduction

The calcium phosphate mineral apatite [$Ca_5(PO_4)_3$(F, Cl, OH)] is a common accessory mineral found in terrestrial magmatic, sedimentary, and metamorphic rocks. Apatite is typically regarded to crystallize in the late stages of magma evolution. Therefore, their formation is believed to be related to magma differentiation or post-magmatic transformation processes. Apatite plays an important role in decipheringthe various geological activities in deep and surface of the planet [1–3]. Given the essential structural hydrogen in apatite, phosphate is widely used to record the abundance of water and volatile concentration of magma [4–11]. Using a U–Pb radioactive decay scheme, apatite can be dated to constrain the ages of the processes.

Gem-quality apatite crystals have been extracted from pegmatites and various magmatic rocks. Granite pegmatite magma, which is peraluminous and volatile-enriched, invades the surrounding rocks and forms pegmatite zones. Rare metals combine with volatiles as ligands and become highly enriched during the late stages of pegmatite crystallization. Apatite, which is a major carrier of volatiles, rare earth elements (REEs, a collective name for scandium (Sc), yttrium (Y), and the lanthanides (La–Lu), and other trace elements, such as Mn, Th, U, and Sr in granitic pegmatites, records information on the magmatic–hydrothermal process of pegmatites. Apatite shows a slight selectivity for middle rare-earth elements (MREEs), with a convex upward mineral/melt partition coefficient pattern. Bai et al. (2021) [12] suggested that the exsolution of Cl fluid from the melts may result in light rare-earth element (LREE) depletion in pegmatite apatite from the Altay Koktokay pegmatitic rare-metal deposit. Mn, Eu, and Ce are redox-sensitive elements

in apatite that could also offer insight into the magmatic oxygen fugacity, i.e., fO_2. Due to its similar radius to iron, Mn^{2+} is more readily able to substitute the site of Ca^{2+} than Mn^{3+} and Mn^{4+}, thus being incorporated into apatite. An increase in Mn^{2+} in reduced magma due to charge transfer leads to an increase in the incorporation of Mn in the apatite structure compared to an oxidized environment. This suggests that the fO_2 condition in silica-rich magma can be constrained by the Mn content of the resulting apatite, independent of other factors such as the melt bulk composition [13]. However, there is no evidence that the fO_2 should be controlled by the apatite melt Mn partitioning in different systems under a broad range of geologically relevant conditions, as suggested by the experiment conducted by Stokes et al. (2019) [14]. Moreover, the experiment data instead showed a dominant role of the melt structure in controlling Mn partitioning [14]. The valence changes in Eu and Ce under different redox conditions infer an alternative method to probe the magmatic fO_2 employed within apatite chemistry [2,11–13]. However, the usage of Eu anomalies as an oxybarometer is largely dependent on the melt bulk composition, as the prior removal of plagioclase from the system can also contribute to Eu anomalies in apatite [15]. Therefore, consideration should be given when interpreting the magmatic fO_2 by apatite.

The incorporation of U and Pb into the apatite lattice enables dating through the radioactive decay system. The closure temperature of the U–Pb apatite system ranges from 350 to 570 °C and is therefore susceptible to heating [16]. It has been reported that the average temperature is 610~900 °C, obtained from the inclusions of the border zone, the first zone, and the third zone of Altay pegmatites [17]. A lower temperature of 480~550 °C was measured in inclusions in spodumenes of Altay pegmatites [18]. However, the mineralization temperature of rare metal pegmatite is mainly within the range of 300 to 550 °C [19]. The temperature at which the minerals are formed is progressively higher from core to rim during the formation of pegmatites, as numerous studies have demonstrated (e.g., [19,20]). In other words, the formation temperature of more evolved pegmatites is higher than that of low evolutionary levels. Therefore, the robustness of the U–Pb system in pegmatite apatite should also be considered concerning the formation temperature of pegmatites in which apatite crystals are formed [21].

Here, we report gem-quality apatite from the Dara-e-Pech pegmatite field in Afghanistan, where literature is sparse compared with apatite of other origins. We investigate the gemological characteristics, including the gemological properties and spectral characteristics, composition, and U–Pb ages, of the pegmatitic apatite. We aim to: (i) compare the gemological and geochemistry characteristics of apatite crystals from different origins, and (ii) constrain the magmatic–hydrothermal evolution and the U–Pb age of Dara-e-Pech pegmatite.

2. Geological Setting

The Dara-e-Pech pegmatite field is a reported economic field located in the province of Kunar, Northeastern Afghanistan (Figure 1). The Dara-e-Pech pegmatite field lies in the Pech Vally, an area that contains economic concentrations of lithium, beryllium, and tantalum, straddling the Nuristan and Kunar provinces. Although the administrative area is delineated in Kunar province, the Dara-e-Pech pegmatite field belongs to the Nuristan Block, which sits on the Hindu Kush–Pamir–Himalayan belt (Figure 1a,b). The Hindu Kush–Pamir–Himalayan belt was formed by a continental collision between the Indian and Eurasian plates. The Indian plate is being subducted beneath the Asian plate, while the Nanga Parbat–Haramosh Massif has been uplifted, forming highly productive pegmatites within the Asian plate, including the famous Nuristan rare-metal pegmatite belt [22]. The Dara-e-Pech pegmatite field is located on the Nuristan rare-melt pegmatite belt (Figure 1c), which is located mainly in the Early Cretaceous (extending from 145 to 100 Ma) Nilau igneous complex, composed of gabbro, monzonite, diorite, and granodiorite (Figure 1c; [23]). Major northeast-trending faults cut and offset portions of this complex. The Dara-e-Pech pegmatite field contains three types of pegmatites:

1. oligoclase–microcline, schorl tourmaline–biotite–muscovite (barren) pegmatite;
2. albitized microcline pegmatite with coarse beryl;
3. spodumene–microcline–albite pegmatite [23,24].

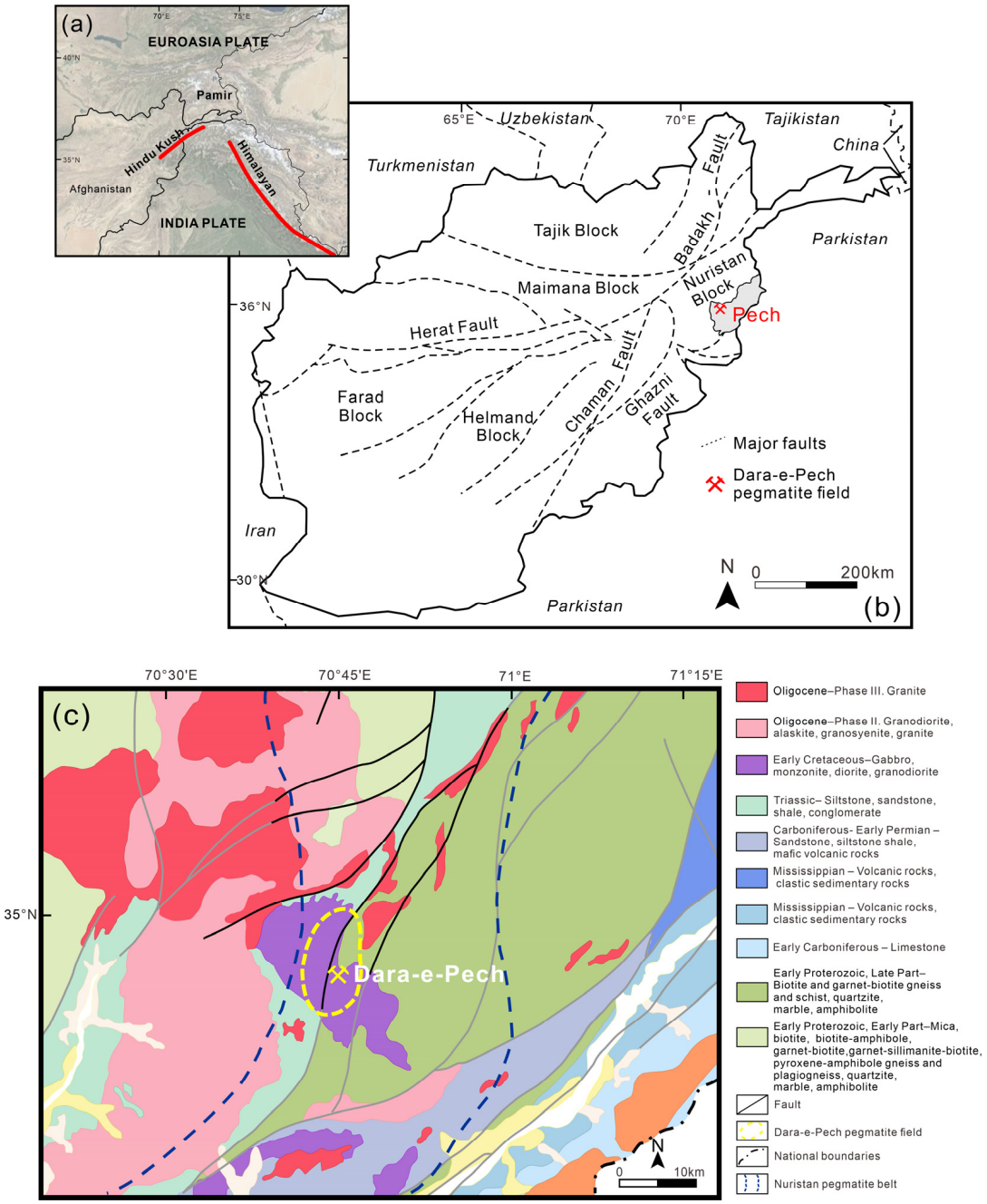


Figure 1. (**a**) Map of regional geology of Afghanistan (modified fromKufner et al. [25]). (**b**) Simplified tectonic map of Afghanistan and noted Dara-e-Pech pegmatite field in Kunar, Afghanistan (modified from Waizy et al. [26]). (**c**) Geologic map of the Dara-e-Pech rare-metal pegmatite area (modified from Cocker [23]).

The pegmatites of Dara-e-Pech have produced flawless crystals of morganite beryl, elbaite, and kunzite. Pegmatites in this area have yielded delicately elbaite specimens, one of which is the green to deep-indigo elbaite "pencils", matching the best from Minas Gerais, Brazil. Additionally, gemmy aquamarine, bi-colored tourmaline, fluorapatite, and topaz have been reported from the Dara-e-Pech pegmatite field [22].

3. Materials and Methods

3.1. Sample Description

Two light-purple hand specimens (Afh-1 to Afh-2) from the Dara-e-Pech pegmatite field in Northeastern Afghanistan were analyzed in this study. The purple apatite developed as aggregates of hexagonal prism crystals with different orientations sitting atop/in the albite matrix embedded within schorl grains (Figure 2a–c). The apatite crystal surface showed shell-like fractures (Figure 2d). The specimens were cleaned and examined using a gemological microscope, revealing the internal features: dark mineral inclusions and fluid inclusions (Figure 2e,f). The apatite crystals were first mechanically crushed into fragments and then selected to be mounted on epoxy resin. They were then polished and carbon-coated to characterize the internal structure using cathodoluminescence (CL) to guide the selection of appropriate locations for in situ chemical composition and in situ isotope analysis. CL images were taken using a Zeiss Merlin compact scanning electron microscope (SEM) located at the Beijing SHRIMP Center, Institute of Geology, Chinese Academy of Geological Sciences. The analytical conditions included an accelerating voltage of 650 kV and a working distance of 13 mm.

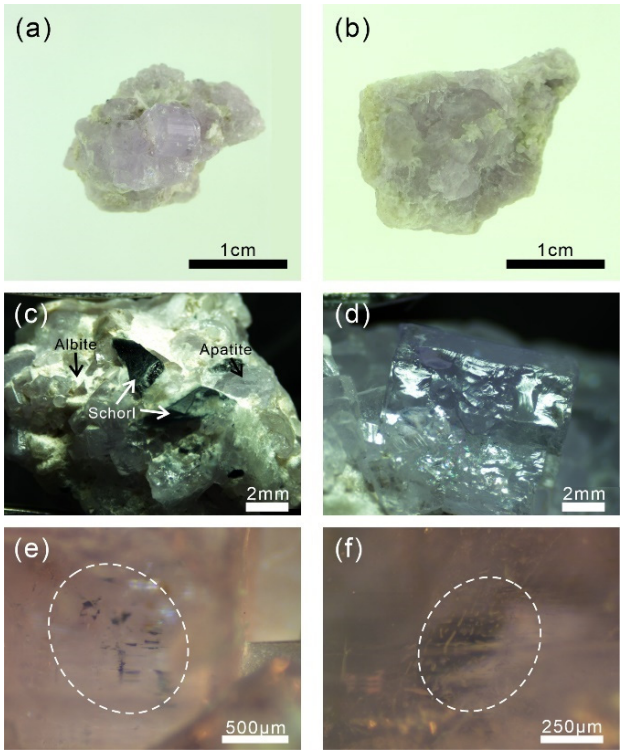


Figure 2. (**a**,**b**) Apatite hand specimens: Afan-1 and Afan-2. (**c**) The mineral assemblage of the apatite samples—apatite crystals stand upon the albite matrix, with some schorl crystals embedded. (**d**) Texture of shell-like fractures under a microscope. (**e**) Dark mineral inclusions inside the apatite (white dotted circle). (**f**) Fluid inclusions inside the apatite (white dotted circle).

3.2. Microscopic Analysis and Spectroscopy

Standard gemological tests of the specimen set were performed at the Gemmological Research Laboratory (GRL) of the China University of Geosciences (Beijing) (CUGB) to determine their refractive index (RI), pleochroism, and fluorescence. The appearance and internal features were examined and captured using a gemological microscope equipped with a camera. The refractive indices were measured on the fine pristine crystal plane or polished surface of apatite using a refractometer. Mercury lamps were utilized to determine the fluorescence reactions to long-wave (365 nm) and short-wave (254 nm) ultraviolet (UV) light. Additionally, the pleochroism was observed using a handheld dichroscope.

The infrared spectra of the Afh-1 and Afh-2 samples were obtained using a reflection method utilizing a Tensor 27 Fourier transform infrared (FTIR) spectrometer (Bruker, Billerica, Germany) at the GRL of the CUGB. Characteristic peaks in the infrared spectra were recorded between 400 and 1500 cm^{-1} with a scanning signal accumulation of 32 times. The temperature and humidity, which can affect the results of the test, were 25 °C and less than 70%, respectively. The scanning voltage was 85–265 V, with a 4 cm^{-1} resolution and a 6 groove/mm grating. Raman spectroscopy was performed using a Horiba LabRAM HR Evolution Raman Spectrometer with a 532 nm laser excitation system (Nd: YAG) at the GRL of the CUGB. The analytic spot sizes were 1 μm depending on the 50×/0.5 objective, and the laser power was ~5 mW. The collected range was 400–1400 cm^{-1}, with a grating of 1800 mm and a 40 s scanning time per point. Prior to collection, a single-crystal silicon wafer was used to calibrate the peak. Polynomial baseline corrections were applied to the collected spectra using LabSpec 6 software.

3.3. Chemical Analysis and U–Pb Dating

An Agilent 7900 quadrupole ICP–MS coupled to the GeoLas HD 193 nm ArF excimer Laser at the Institute of Geomechanics, Chinese Academy of Geological Sciences Institute of Geology, Beijing, was used to acquire both the trace element (TE) and U–Pb data of the Afghanistan apatite samples. The laser was fired at a repetition rate of 5 Hz and a fluence of 2.3 J/cm^2 using spot sizes of 32 and 60 μm for the TE and isotope measurements, respectively. Each acquisition consisted of 15 s of blank measurement, followed by TE signal measurement for another 20 s, with 30 s of wash time between each analysis. NIST SRM610 was used as a reference material to calibrate the time-dependent drift and mass discrimination. Other external reference materials used for in situ analysis were NIST SRM612 silicate glass and McClure apatite. ^{43}Ca was used as an internal standard for phosphates. Madagascar apatite (MAD) (485.2 ± 0.8 Ma after common Pb correction, a Th/U ratio of ~26, $^{206}Pb/^{238}U$ = 0.0762, and $^{207}Pb/^{235}U$ = 0.6013) was used as the external isotope calibration standard [27,28]. The isotopic ratios and uncertainties for individual analyses are quoted with the 2 s level (Table A2). Data reduction was processed following the methods reported by Chew et al. [29] using the Isoplot program [30]. Due to the high common Pb levels in apatite, a Tera–Wasserburg plot was used to anchor the common Pb composition, with a $^{208}U/^{206}Pb$ lower intercept age. The ^{207}Pb-corrected $^{208}U/^{206}Pb$* age (* represents radiogenic value) was analyzed using ISOPLOT [30].

4. Results

4.1. Gemological Properties

The RI values were 1.631–1.633 for a birefringence (Δn) of 0.002. Some gemological properties, such as hydrostatic specific gravity (SG), were not measured due to their inconvenient measurement with the matrix. When viewed using a dichroscope, the purple samples showed weak–moderate pleochroism from pastel to light pinkish purple. All of the samples reacted to the long-wave UV light with a moderate pinkish purple fluorescence reaction and were inert to short-wave UV.

4.2. Spectroscopy

4.2.1. FTIR Spectra

The infrared spectral vibrations of the apatite in the wave number range from 400 to 1500 cm^{-1} mainly showed four kinds of vibrations of PO_4^{3-}, which included ν_1 symmetric stretching vibration, ν_2 bending vibration, ν_3 asymmetric stretching vibration, and ν_4 bending vibration.

The FTIR spectra recorded from the Afghanistan samples displayed characteristic double broad bands near 1060 cm^{-1} and 1109 cm^{-1}, which can be attributed to ν_3 asymmetric stretching vibration. In the region of 550–650 cm^{-1}, all the samples showed medium–strong double peaks near 576 cm^{-1} and 607 cm^{-1}, which were assigned to the ν_4 bending vibrations of the phosphate group. The ν_1 P–O stretching IR mode appeared at ~962 cm^{-1} in

the spectra (Figure 3a). The 468 cm^{-1} peak is believed to be related to the ν_3–ν_4 differential band vibrations [31], while some opinions have assigned it to a ν_2 bending vibration [32]. The peaks activated by CO_3^{2-} ions at 1415, 879, and 680 cm^{-1} were absent, which indicates negligible carbonate in our sample [33]. Research by Hammerli et al. [34] suggests the possibility of volatile concentration determination via attenuated total reflection–Fourier transform infrared spectroscopy (ATR-FTIR). However, the H_2O in our sample was difficult to accurately quantify due to a lack of credible calibration.

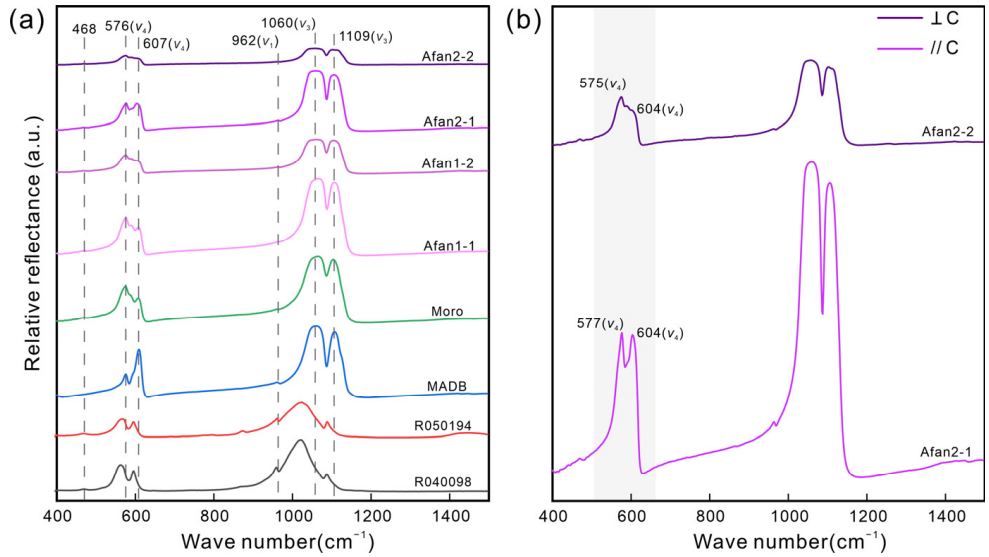


Figure 3. (**a**) Infrared spectra of the Afghanistan apatite and other samples (R050194 and R040098 from the RRUFF database, MADA from Zhang et al. [35], and Moro from Yuan et al. [36]). (**b**) Infrared spectra of the Afghanistan apatite tested in different orientations.

Figure 3b shows the differences in the intensity of the peaks within the range of 550–650 cm^{-1}. The measurements were conducted on the prismatic and basal orientation of the crystals to determine the differences in the spectra. The spectra plotted in Figure 3b show that the peak of the crystals near 604 cm^{-1} was stronger than the peak near 576 cm^{-1} when oriented with the c-axis perpendicular to the beam. However, the result is opposite when the c-axis of the apatite crystals is parallel to the beam, as revealed by the spectra. The conclusion can be drawn that the IR spectra peaks ranging from 550 to 650 cm^{-1} helped to identify the orientation of the apatite crystal.

4.2.2. Raman Spectra

Figure 4a demonstrates that the strongest peak of the Afghanistan apatite samples was 964 cm^{-1}, corresponding to the ν_1 symmetric vibration of $[PO_4]^{3-}$ [37,38]. In the region of the ν_2 bending mode, a moderately strong peak appeared at 430 cm^{-1} [33]. It has been proposed that the ν_4 $[PO_4]^{3-}$-related peaks located from 400 to 650 cm^{-1} can be used for discriminating between hydroxyapatite, fluorapatite, and hydroxyfluoraptite because of its sensitivity to the proportions of OH^- and F in apatite [39]. Fluorapatite only has bands located at 591 and 608 cm^{-1}, while hydroxyfluorapatite has four bands at 581, 592, 608, and 617 cm^{-1} [40]. Additionally, in the region from ~3300 to 3600 cm^{-1}, OH with different adjacent anions shows different Raman peaks, including hydroxyl (band at ~3575 cm^{-1}), fluorine (band at ~3535–3540 cm^{-1}), and chlorine (band at ~3494 cm^{-1}) [39,41,42]. The spectra of the Afghanistan apatite samples demonstrated moderate peak bands at 590 and 606 cm^{-1}, which suggests that the samples were fluorapatite rather than hydroxyfluorapatite (Figure 4a). In the spectral range of O–H stretching vibrations, the band peak at 3538 cm^{-1} also suggests the existence of F–OH solid solution [41,43].

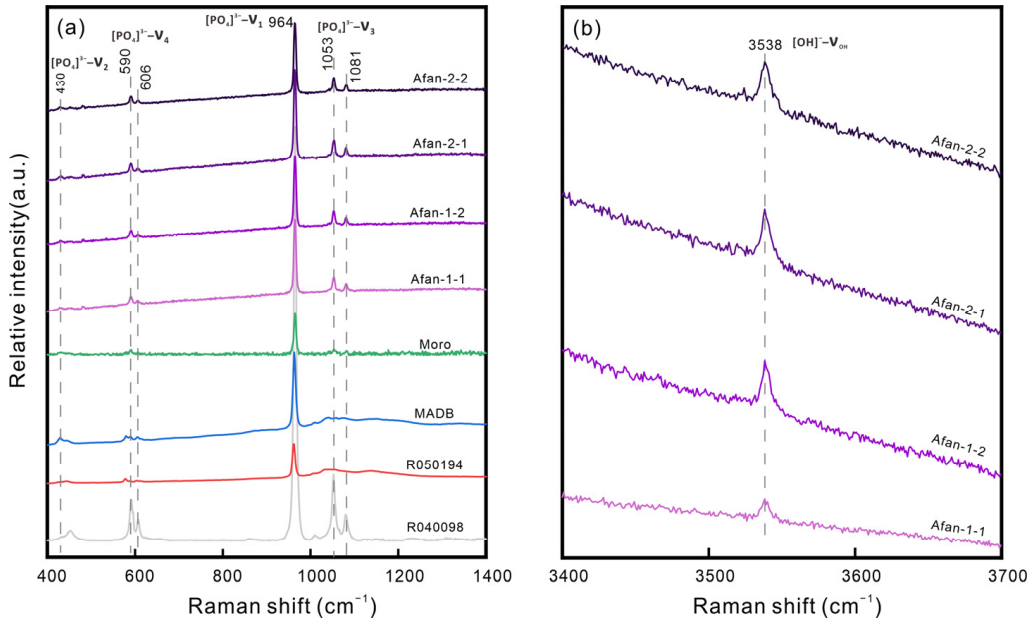


Figure 4. (**a**) Raman spectra of Afghanistan apatite samples compared to those of R050194 (a pure apatite from RRUFF database), R040098 (Durango apatite from RRUFF database), MADA [35], and Moro [36]. (**b**) Raman spectra of Afghanistan apatite crystals within the range of 3400–3700 cm^{-1}.

The weak absorption bands near 1053 and 1081 cm^{-1} were attributed to ν_3 asymmetric stretching vibration (Figure 4a; [37]). Carbon-related bands at 737 cm^{-1} (CO_3^{2-} ν_4) [44] and 1070 cm^{-1} (CO_3^{2-} ν_1) [45] were not observed, indicative of the absence of CO_3^{2-} in the apatite lattice in any significant amount, which is consistent with the IR spectra. There were no peaks in the 640–672 cm^{-1} region, suggesting a sign of low SO_4^{2-} content [40].

4.3. Trace Element Compositions

The analyzed spots used for trace element composition are demonstrated in Figure 5. The results are shown in Figure 6a and Table A1. The samples had a wide variation in Y and Sr content (Sr: 698.59–3910.69 μg/g Sr; Y: 133.52–906.38 μg/g). The ΣREE values in the apatite were in the ranges 64.41 to 729.06 μg/g, with ΣLREE values of 2.07 to 73.62 μg/g and ΣHREE values of 62.06 to 655.43 μg/g. The CI-normalized REE patterns displayed obvious REE fractionation, with intense HREE enrichment ($(LREE/HREE)_N$ = 0.04–0.15) and strong LREE depletion (Figure 6a). The purple samples showed negative Eu anomalies (δEu = Eu/Eu*: 0.59–0.95) and both positive and negative Ce anomalies (Ce/Ce* = 0.67–1.15).

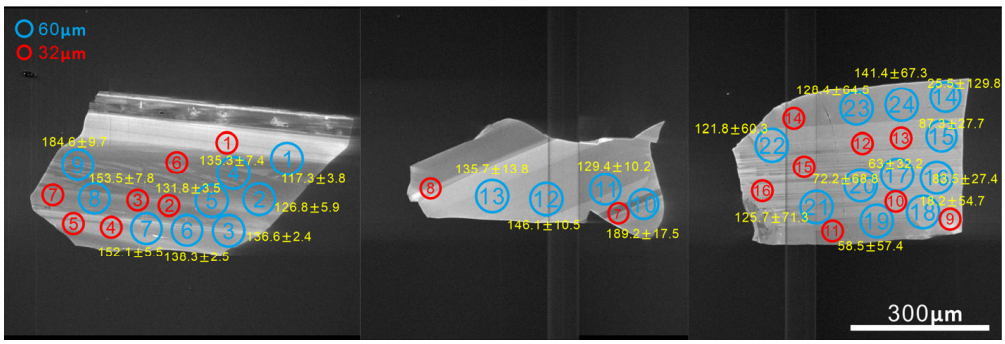


Figure 5. Cathodoluminescence (CL) images of apatite from Afghanistan. Red circles with a spot size of 32 μm show positions for LA-ICP-MS trace element analyses. Blue circles with a size of 60 μm represent the positions for LA-ICP-MS U–Pb dating analyses, and the yellow annotations represent $^{206}Pb/^{238}U$ ages after ^{207}Pb correction.

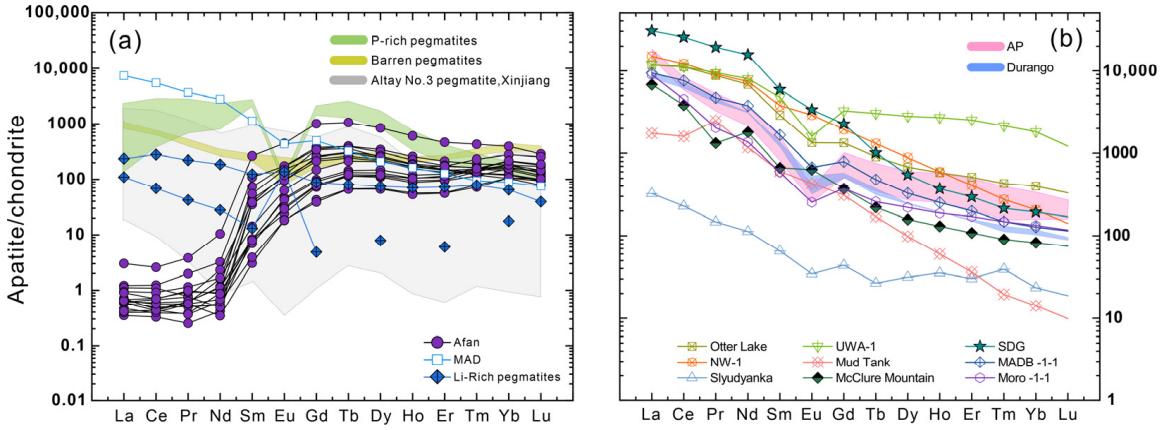


Figure 6. Chondrite-normalized REE patterns of apatite (**a**) from Afghanistan and (**b**) other localities (references are listed in Section 5.1.3) (McDonough and Sun [46]).

4.4. U–Pb Age

A total of 24 spots on the apatite samples were analyzed during the LA-ICP-MS U–Pb dating. The in situ U–Pb isotope ratios measured are shown in Table A2. The U content ranged from 3.74 to 119.52 μg/g, and the Th content ranged from 0.17 to 40.39 μg/g, with an average Th/U of 0.38. Due to the high and variable common Pb component in the apatite grains, the isotopic data are presented on a Tera–Wasserburg diagram with an anchored $^{207}Pb/^{206}Pb$ value of 0.5948 ± 0.0026 and a lower $^{238}U/^{206}Pb$ intercept at 135.8 ± 6.9 Ma (MSWD = 1.3; n = 24; Figure 7a). The weighted mean ^{207}Pb-corrected $^{238}U/^{206}Pb$* age was 135.0 ± 6.0 Ma, with an MSWD of 4.3 (n = 11; Figure 7b). Although accurate ages are difficult to obtain due to a high common Pb content, all of the ages were consistent with the formation time of the Nilau igneous complex (145–100 Ma) where the analyzed samples were produced. Therefore, the lower intercept age could represent the timing when our samples crystallized.

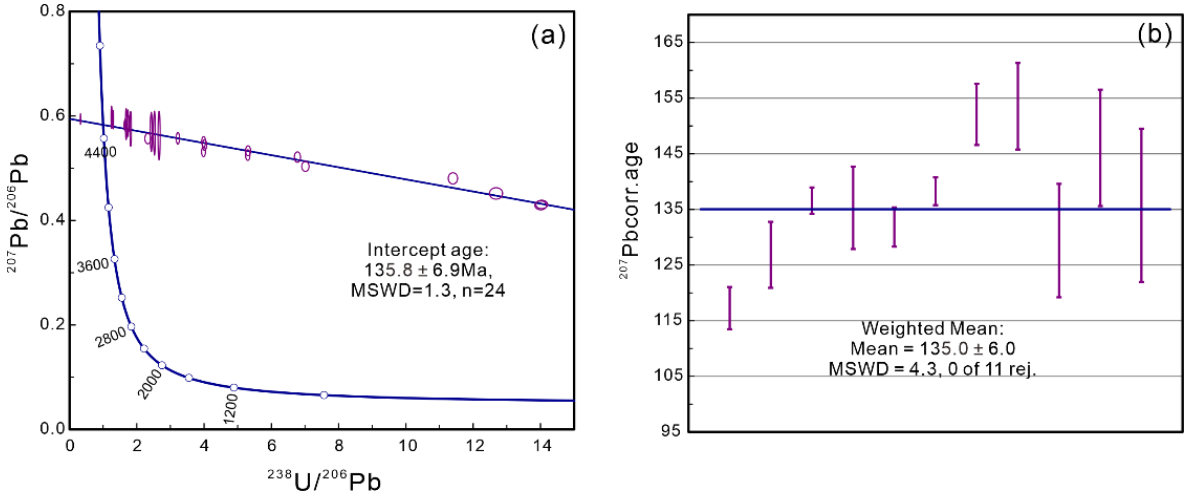


Figure 7. (**a**) Tera–Wasserburg U–Pb concordia diagram of apatite from Afghanistan. Regression line envelops are 2s uncertainties. (**b**) ^{207}Pb-corrected average ages with 2s uncertainties.

5. Discussion

5.1. Origin Identification

In this research, the spectral characteristics of apatite produced in Afghanistan were compared with samples from various origins, including Durango from Mexico, blue apatite from Madagascar [35], and greenish-yellow apatite from Morocco [36]. The Afghanistan

apatite was determined as fluorapatite according to the Raman spectra. It is reported that the comparative apatite from Mexico, Madagascar, and Morocco are F-apatite as well [35,36,47]. The fluorapatite R050194 from the RRUFF database, produced in the Siglo XX deposit in the Larragua region of Bolivia, was selected in order to compare the differences in the IR spectra and Raman spectra. The standard material R050194 was confirmed as pure fluorapatite with the measured chemical formula of $Ca_{5.00}(P_{1.00}O_4)_3F_{1.00}$. R050194 is therefore suitable for comparative analysis with the Afghanistan, Madagascar, and Morocco samples.

5.1.1. Infrared Spectra Comparison

The infrared absorption spectra of all the samples shared similarities at the main band peaks, suggesting consistencies in the molecular structures (see Figure 3a). The parameters of the doublet ~1060 and ~1109 cm^{-1}, corresponding to the ν_3 antisymmetric stretching vibration, significantly red-shifted and broadened compared with previous studies [34,35]. The ν_3 vibrations in the IR spectra of the fluorapatite appeared at 1029 and ~1095 cm^{-1}, which were significantly different from the samples in this study, as reported by Zolotarev et al. (2018) [48] A study by Ulian [49] suggests that an increase in apatite structural defects and a decrease in the crystallinity broaden the ν_3 band and reduce its intensity. The relatively abundant inclusions and developed fractures, as described previously, would increase the likelihood of crystal structural defects. It can be seen that the ν_3 bands of the apatite from other origins were significantly broadened (with respect to the spectrum obtained from R050194 fluroapatite), suggesting more structural defects in the lattice.

5.1.2. Raman Spectra Comparison

The peak positions of the ν_1 $[PO_4]^{3-}$ vibration of all the comparative apatite crystals were consistent with R050194 from the RRUFF database. It has been reported that the ν_1 symmetry vibration in the Raman spectrum, similar to asymmetric vibrations ν_3 in IR absorption spectrum, is susceptible to structural imperfections in the apatite lattice and its crystallinity [32,33]. An increase in structural defects and a decrease in the crystallinity result in an increase in the half-width $\Delta\nu1$ of the ν_1 band by a factor of 2–3 and a red-shift of ~5 cm^{-1}, as reported by Zolotarev et al. (2018) [48]. However, no obvious difference in the frequency shift was observed in the apatite crystals from Afghanistan or other origins (Figure 4a), indicative of their good crystallinities.

5.1.3. Trace Element Characteristics

In this section, apatite from various localities and generation environments are compared with the Afghanistan apatite, including AP (probably from Madagascar) [50], Otter Lake (Canada) from calcite [50], NW–1 (Ontario) from alkaline carbonatite [50], Slyudyanka (Lake Baikal) from metamorphic siliciclastic carbonate phosphogypsum [50], Durango (Mexico) from ion deposits [50], UWA–1 (Bancroft, Ontario) [50], Mud Tank (Austalia) from carbonatite [50], McClure Mountain (Colorado) from anorthite [50], SDG (Inner Mongolia, China) from alkaline ultramafic rocks [50], MADB (Madagascar) [35], and Moro (Anemzi, Morocco) [36]. Pegmatitic apatite from Madagascar (MAD) [38], the Central Iberian zone (CIZ) [51], and Xinjiang (Altay No.3 pegmatite) [52,53] are also used for origin identification.

Although the Sr–Y plot is not optimal for use to discriminate the host rocks of apatite, it can provide information on the magma fractionation, as the Sr concentrations decrease while the Y concentrations increase with magma differentiation [1,54]. Pegmatitic apatite from Li-rich pegmatites of CIZ show a broader range, displaying very high contents of Sr (4366–7610 μg/g) but low contents of Y (24–134 μg/g), which is consistent with the highly fractionation magma source. As shown in Figure 8, Afghanistan apatite shows a negative correlation between its Sr and Y contents, indicating an evolving trend of its magma source, while apatite from Altay pegmatites exhibits a positive correlation, of which have the Sr and Y contents range from 6.46 to 317.14 μg/g and 672.94 to 3.87 μg/g, respectively (Table A3).

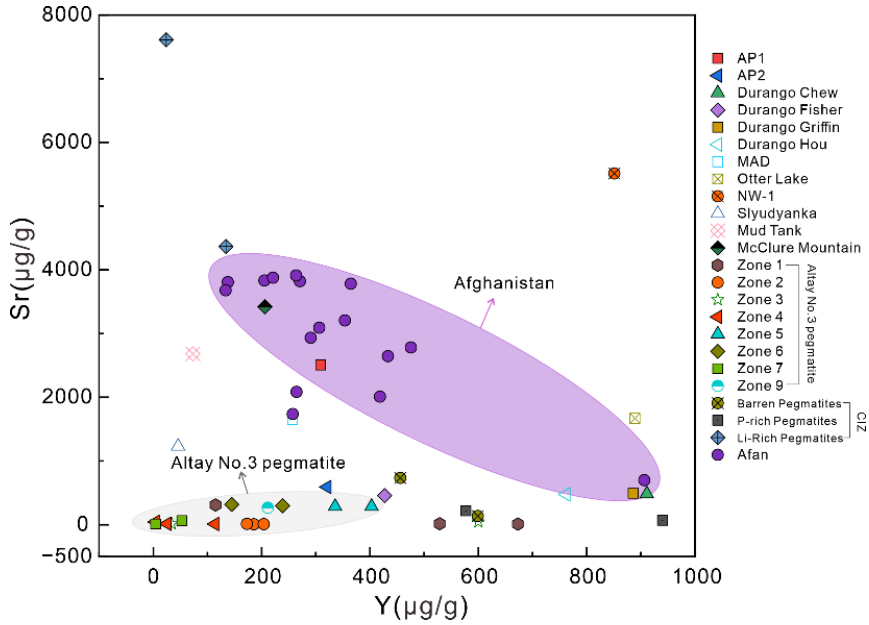


Figure 8. Y vs. Sr in apatite from Afghanistan and various localities.

All the apatite from the other localities showed various degrees of LREE enrichment ($(Ce/Yb)_N$) ranging from 1.49 to 131.89), while the Afghanistan apatite showed $(Ce/Yb)_N$) < 0.01 with ratios ranging from 0.001 to 0.007 (Figure 6; Tables A1 and A3). It has since been reported that hydrothermal exsolution of Cl-containing fluids could lead to depleted LREE in apatite, which may infer the genesis of HREE enrichment in Afghanistan apatite [54]. AP, MAD, Mud Tank, SDG, NW–1, and MADB apatite showed strong HREE depletion ($(Ce/Yb)_N$: 58.40–131.89), while one apatite from the fifth zone of Altay No.3 pegmatite showed less LREE enrichment, with $(Ce/Yb)_N$ = 1.49.

Most apatite crystals have clear negative Eu anomalies, with Eu/Eu* = 0.04–0.94. Except for the MAD and apatite from Li-rich pegmatites (CIZ), the other pegmatite apatite crystals showed strong negative Eu anomalies (δEu < 0.5), while the Afghanistan pegmatite apatite exhibited weak negative Eu anomalies (δEu = Eu/Eu*: 0.59–0.95; Figure 6; Table A3). Only the McClure Mountain apatite and apatite from Li-rich pegmatites (CIZ) showed positive Eu anomalies. One apatite from the Li-rich pegmatites of CIZ showed a prominent negative Eu anomaly, with a δEu of 15.4. The NW–1 apatite exhibited almost no Eu or Ce anomalies, of which the δEu and δCe values were both 1.01. Based on the chondrite-normalized REE patterns, Ce anomalies were subtle to absent with range from slightly negative to slightly positive, with the exception of one apatite from the Altay third zone and two apatites from the Altay fourth zone, which showed moderate negative Ce anomalies (δCe = Ce/Ce*: 0.55–0.67; Table A3).

5.2. Oxidation State of Apatite

REEs (typically present as 3+ cations) are readily incorporated into apatite; however, Eu and Ce can be present as either 2+ or 3+ cations. Apatite crystals prefer incorporating Eu^{3+} and Ce^{3+} over Eu^{2+} and Ce^{4+} due to the proximity of their ionic radii to Ca^{2+}, resulting in anomalies in the Eu and Ce contents relative to other (trivalent) REEs, which can be used to probe the magmatic fO_2 of apatite. The reducing conditions may lead to negative Eu anomalies in apatite because of the Eu^{3+}/Eu^{2+} transition. It is noteworthy that the separation of feldspar before apatite, which has strong affinities to Eu and Sr and subsequently depletes the Eu and Sr contents of both magma and apatite, is assumed to affect the use of apatite as a direct oxybarometer. Ce anomalies in apatite, however, are thought to be relatively independent of crystallization effects, except for zircon or accessory REE-rich phases. Although apatite shows various extents of Ce anomalies, the extents

themselves are subtle. The apatite analyzed in this study showed weak to intermediate negative Eu anomalies (δEu = Eu/Eu*: 0.59–0.95; Table A1). According to previous studies, the negative anomalies in apatite can be attributed to either the crystallization of plagioclase or low magmatic fO_2.

For the first case, the Sr and REE contents of apatite are believed to be able to reflect the magma evolution process of apatite and plagioclase, as mentioned above. It has been reported that the positive correlations between Sr–$(La/Yb)_N$ and Sr–$(Sm/Yb)_N$ indicate the simultaneous crystallization of apatite and plagioclase or late crystallization of apatite after plagioclase [50,52]. However, the Sr content of the Afghanistan samples was negatively correlated with apatite $(La/Yb)_N$ and $(Sm/Yb)_N$, suggesting a less dominant role of feldspar crystallization in the magmatic differentiation process (Figure 9).

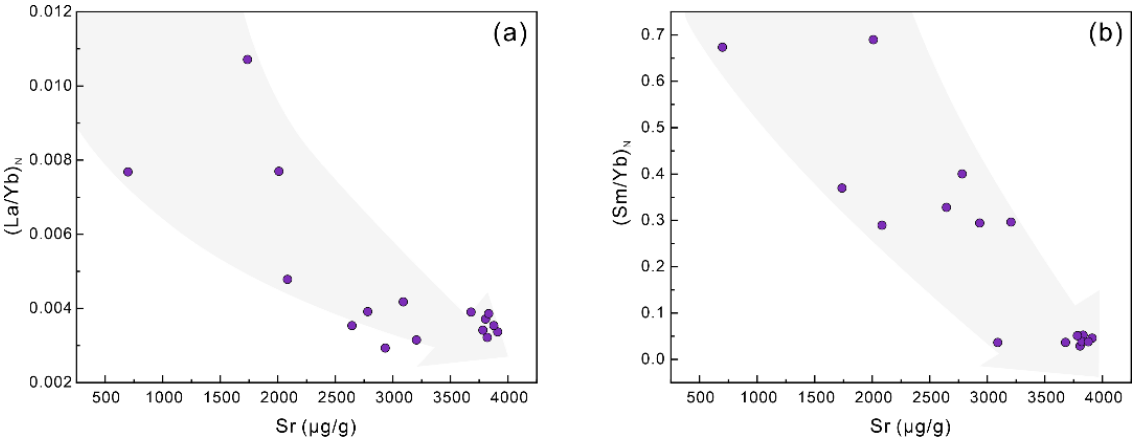


Figure 9. (**a**) Sr vs. $(Sm/Yb)_N$ in apatite from Afghanistan. (**b**) Sr vs. $(La/Yb)_N$ in apatite from Afghanistan.

For another case, a δCe verse δEu plot is demonstrated to reflect the degree of magma redox and oxygen escape (Figure 10). It has been reported that the feature of Eu anomaly is barely affected by the crystallization of feldspar during a magmatic–hydrothermal process [12]. Subsequently, the heavy Eu anomalies of apatite from Altay No.3 pegmatites may indicate a reduced pegmatitic magma, except for one apatite from Zone 1 and apatite from Zone 6, which display moderate oxidized conditions [52]. P-rich pegmatite apatite were suggested to formed under reducing conditions and had nothing to do with the coexisting plagioclase confirmed by petrographic observation [51]. Apatite found in barren pegmatite correspond to higher oxygen fugacity, and apatite found in Li-rich pegmatite correspond to more oxidized conditions (Figure 10; [51]). Compared to the other pegmatite apatite, the Afghanistan apatite showed intermediate Eu anomalies and subtle Ce anomalies, which could be attributed to a moderately oxidized magmatic environment.

5.3. Source and Process of Mineralization Based on Apatite Characteristics

Although controversies concerning the sources, composition, temperature, and pressure conditions and the evolution process of the related ore-forming fluid need more evidence to solve, the formation mechanisms of granite pegmatite-type rare metal deposits have been well-studied. One mainstream opinion considers the highly fractionated granitic magma as another attribute of the small proportion of rare-metal-rich sources deep melting.

Elements of similar charge and ionic radius should display a high degree of coherent behavior in geochemical systems characterized by charge and radius controlled (CHARAC) behavior, such as Y–Ho and Zr–Hf [53,55]. The Y–Ho ratios of basic to intermediate igneous rocks show CHARAC behavior and are close to that of the chondrites (Y/Ho = 24~34). However, in highly evolved magma, Y and Ho behave like they are in aqueous media and combine with ligands (e.g., non-bridging oxygen (NBO), F, and B), which infers high-silica magmatic systems rich in H_2O, Li, B, F, P, and/or Cl between pure silicate melts and hydrothermal fluids [53,55]. The Y–Ho ratios of the Afghanistan apatite samples

ranged from 24.8 to 52.1, which indicates the decoupling of Y and Ho, indicating that the samples formed in a transitional magmatic–hydrothermal system (Figure 11; Table A1). Additionally, the negative correlation between Sr and Y contents indicates an evolving trend of magma. Kunzite, which is found in the Dara-e-Pech rare metal field, is considered as an indicator of relatively evolved pegmatites [19].

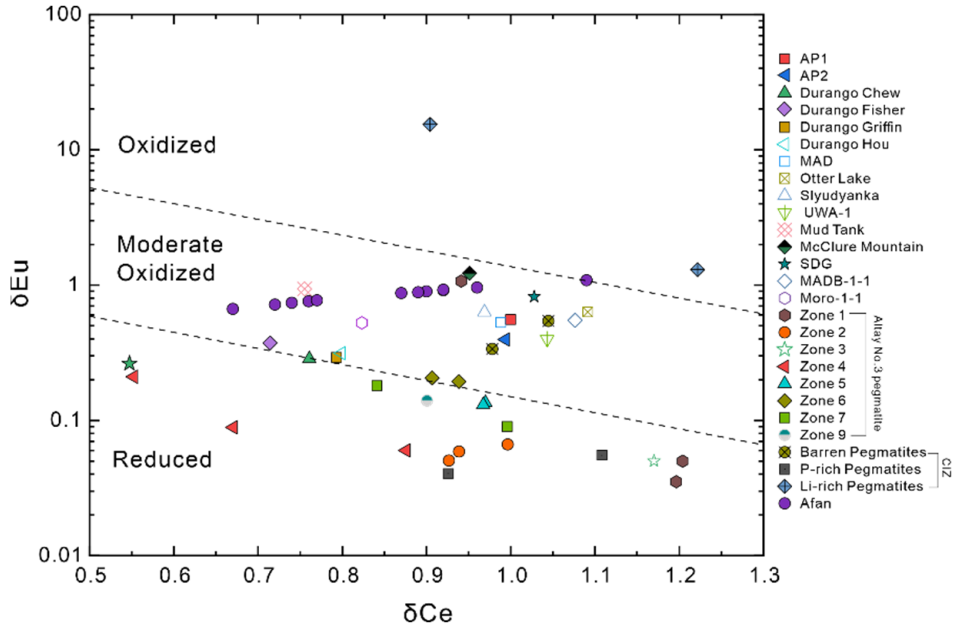


Figure 10. δCe vs. δEu in apatite from Afghanistan and other localities.

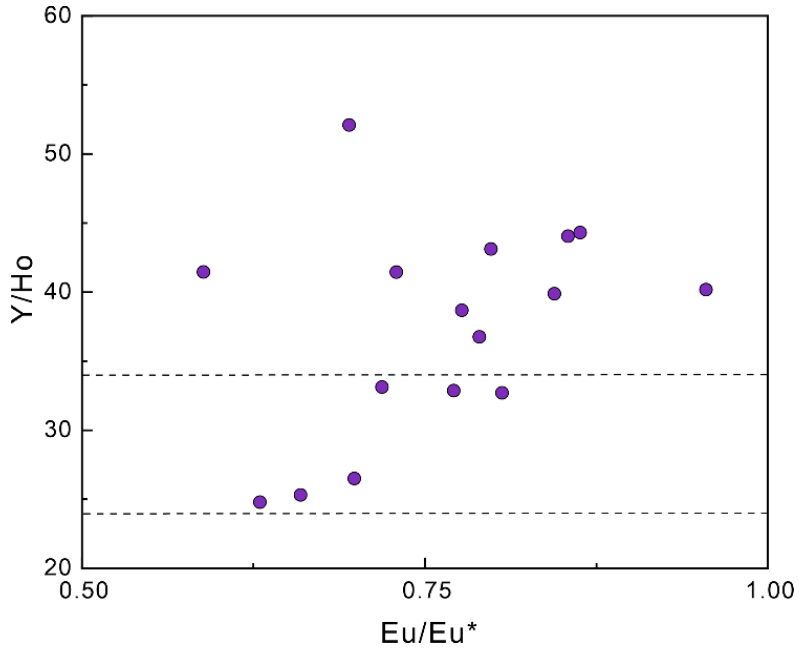


Figure 11. Eu/Eu* vs. Y/Ho in apatite from Afghanistan. The dashed lines decide the range of 24–34, which represents the Y/Ho ratios of the chondrites.

The Sr contents in apatite have been reported as very low (<100 μg/g) in highly evolved granitoid and granite pegmatites; however, the Y contents can be over 1% [1]. The ranges of Sr and Y concentrations of the Afghanistan apatite were 698.59–3910.69 μg/g and 133.52–906.38 μg/g, respectively, while the ranges of Altay pegmatites were 6.46–317.14 μg/g and 672.94–3.87 μg/g, respectively (Tables A1 and A3). The Sr contents in the Afghanistan

apatite showed a negative correlation with the Y contents, in contrast to the positive correlation found in Altay pegmatite apatite (revealed in Figure 8). Therefore, it can be inferred that the Altay pegmatites formed in a more evolved granitic environment than the Afghanistan pegmatites where the studied apatite formed.

The temperature of the ore-forming fluid increases during the fractionation of pegmatitic magma [19,20]. the less-evolved Afghanistan apatite is supposed to have a lower temperature than the temperature measured by the inclusions of Triassic Altay pegmatites within the range of 400 to 581 °C. The closure temperature for Pb diffusion in apatite ranges from 350 to 570 °C, which is less likely to be influenced by heating, as the mineralization of rare metal deposits mainly happens at 300 to 500 °C [19]. All the rare-metal pegmatites of the pegmatite belt of Afghanistan are the product of magmatic residual liquid, as reported by Ahmadi et al. (2018) [24]. Nilau igneous complex intrudes the Early Proterozoic (2500–541 Ma) and Triassic (201–252 Ma) rocks and forms the Dara-e-Pech rare metal field. The LA-ICP-MS U–Pb age of the purple Afghanistan apatite is 135.8 ± 6.9 Ma, which may represent the age of magmatic hydrothermal growth when the magmatic residual liquid of Nilau igneous complex was intruded the Early Proterozoic and Triassic rocks.

6. Conclusions

Apatite from the Dara-e-Pech pegmatite field can be easily discriminated from other origins (Durango from Mexico, Morocco, and Madagascar) based on its gemological properties and composition. Non-CHARAC ratios of Y–Ho (24.8–52.1) indicate that the samples crystallized in a transitional magmatic–hydrothermal system rich in H_2O, Li, B, F, P, and/or Cl. The intermediate Eu anomalies and subtle Ce anomalies imply that the apatite formed in moderately oxidized magma. Additionally, the negative correlation between the Sr and Y contents in the Afghanistan apatite indicates an evolving trend of magma. However, compared with apatite from Altay pegmatites, which contain lower S but higher Y contents, the Dara-e-Pech pegmatite field apatite formed a relatively less-evolved granitic pegmatite environment. Therefore, the ore-forming fluid of the Dara-e-Pech pegmatite field had a lower forming temperature than Altay pegmatites (400–581 °C), and the U–Pb system is retained without being affected by heating. The U–Pb age derived from the apatite samples was 135.8 ± 6.9 Ma, which may represent the age of the magmatic–hydrothermal activity when the Dara-e-Pech pegmatite field formed in magmatic residual liquid.

Author Contributions: Writing—original draft, B.L.; writing—review and editing, B.L., B.X. and Y.Z.; data curation, B.L.; software, B.L.; methodology, B.X. and Y.Z. All authors have read and agreed to the published version of the manuscript.

Funding: This research was funded by the National Natural Science Foundation of China (42222304, 42073038, 41803045, 42202084), Young Talent Support Project of CAST, the Fundamental Research Funds for the Central Universities (Grant no. 265QZ2021012), and IGCP-662.

Data Availability Statement: The data presented in this study are available within the article.

Acknowledgments: We thank the editors and two anonymous reviewers for their constructive comments which helped in improving our paper. This is the 25th contribution of B.X. for the National Mineral Rock and Fossil Specimens Resource Center. This work was supported by the National Key Research and Development Program of China (grant 2022YFF0704901) and the National Natural Science Foundation of China (grant 42241158).

Conflicts of Interest: The authors declare no conflict of interest.

Appendix A

Table A1. Trace element composition for apatite of the pegmatite from the Dara-e-Pech pegmatite field (value in μg/g).

Spot	Afan-01	Afan-02	Afan-03	Afan-04	Afan-05	Afan-06	Afan-07	Afan-08	Afan-09	Afan-10	Afan-11	Afan-12	Afan-13	Afan-14	Afan-15	Afan-16
Rb	0.07	0.00	0.08	0.00	0.00	0.06	0.06	0.00	0.19	0.10	0.00	0.12	0.00	0.06	0.08	0.13
Sr	698.59	3205.60	2781.76	2009.55	2644.78	2084.35	2933.83	1737.00	3805.73	3832.20	3679.27	3820.96	3910.69	3782.13	3877.25	3090.78
Y	906.38	353.79	475.74	418.39	433.09	264.51	290.74	257.41	137.84	205.28	133.52	270.75	263.83	364.75	221.03	306.50
La	0.71	0.11	0.17	0.29	0.14	0.14	0.08	0.26	0.09	0.15	0.10	0.16	0.15	0.23	0.15	0.21
Ce	1.58	0.24	0.27	0.75	0.26	0.30	0.20	0.67	0.24	0.42	0.26	0.44	0.37	0.56	0.34	0.43
Pr	0.36	0.04	0.06	0.19	0.06	0.05	0.02	0.07	0.05	0.07	0.03	0.09	0.06	0.11	0.05	0.09
Nd	4.86	0.42	0.54	1.50	0.75	0.25	0.19	1.08	0.16	0.23	0.29	0.42	0.52	0.77	0.32	0.40
Sm	40.40	6.68	11.20	16.61	8.33	5.44	5.36	5.84	0.47	1.27	0.60	1.25	1.28	2.18	1.07	1.21
Eu	25.72	6.31	9.88	10.09	8.72	5.50	5.56	6.92	1.05	1.38	1.06	2.63	2.48	3.67	1.82	1.69
Gd	206.64	47.61	71.83	77.19	53.54	51.75	43.95	69.96	8.69	14.86	7.93	20.35	18.81	30.53	16.23	15.58
Tb	39.61	9.82	14.77	14.59	11.49	11.12	9.07	13.36	2.51	4.30	2.48	5.41	4.98	8.00	4.29	4.55
Dy	213.60	57.99	87.13	78.60	67.05	62.57	54.88	63.58	17.47	27.92	16.86	37.69	33.28	53.12	29.40	30.47
Ho	34.20	9.62	14.55	12.63	10.78	10.45	8.85	10.38	3.20	4.95	3.01	6.79	5.99	9.43	5.33	5.88
Er	76.56	24.17	35.15	29.54	28.39	25.39	22.20	24.67	9.44	15.72	9.26	20.71	18.01	28.65	16.16	19.17
Tm	10.90	3.90	4.88	4.07	4.19	3.32	3.26	3.08	2.00	2.95	1.84	3.93	3.84	5.86	3.53	4.01
Yb	66.65	25.07	31.10	26.77	28.20	20.89	20.22	17.56	17.99	27.00	18.08	36.02	31.10	47.35	31.29	36.74
Lu	7.28	2.81	3.29	2.99	3.44	2.53	2.43	1.99	2.38	3.69	2.60	4.59	4.34	6.44	3.71	4.76
Hf	0.00	0.00	0.00	0.01	0.00	0.01	0.01	0.00	0.00	0.02	0.02	0.02	0.00	0.00	0.00	0.00
Y/Ho	26.50	36.76	32.71	33.12	40.17	25.31	32.87	24.79	43.12	41.46	44.31	39.88	44.05	38.68	41.44	52.09
ΣLREE	73.62	13.79	22.13	29.44	18.25	11.67	11.42	14.84	2.07	3.51	2.35	4.99	4.85	7.51	3.76	4.04
ΣHREE	655.43	181.00	262.70	246.37	207.07	188.03	164.85	204.58	63.68	101.40	62.06	135.49	120.35	189.39	109.94	121.17
ΣREE	729.06	194.79	284.83	275.81	225.32	199.70	176.27	219.42	65.75	104.91	64.41	140.48	125.20	196.90	113.70	125.21
$(LREE/HREE)_N$	0.14	0.11	0.12	0.15	0.13	0.09	0.10	0.10	0.04	0.04	0.04	0.05	0.05	0.05	0.04	0.04
$(Ce/Yb)_N$	0.01	0.00	0.00	0.01	0.00	0.00	0.00	0.01	0.00	0.00	0.00	0.00	0.00	0.00	0.00	0.00
Eu/Eu *	0.70	0.79	0.81	0.72	0.95	0.66	0.77	0.63	0.80	0.59	0.86	0.84	0.85	0.78	0.73	0.69

Table A1. *Cont.*

Spot	Afan-01	Afan-02	Afan-03	Afan-04	Afan-05	Afan-06	Afan-07	Afan-08	Afan-09	Afan-10	Afan-11	Afan-12	Afan-13	Afan-14	Afan-15	Afan-16
Ce/Ce *	0.76	0.92	0.67	0.77	0.72	0.90	1.09	1.15	0.83	0.99	1.11	0.89	0.96	0.87	0.92	0.74
Th/U	0.10	0.05	0.10	0.23	0.05	0.38	0.09	1.54	0.38	0.45	0.36	0.49	0.48	0.55	0.45	0.3

Note: ΣREE: the sum concentration of the lanthanides (from La to Lu); ΣLREE: the sum concentration of the lanthanides (from La to Eu); ΣHREE: the sum concentration of the lanthanides (from Gd to Lu); $Eu/Eu^* = 2Eu_N/(Sm_N + Gd_N)$; $Ce/Ce^* = 2Ce_N/(La_N + Pr_N)$.

Table A2. Apatite U–Pb dating using LA-ICP-MS.

Spot	Th	U	Th/U	Pb_{total}	$^{206}Pb/^{238}U$	1s	$^{207}Pb/^{206}Pb$	1s	$^{207}Pb/^{235}U$	1s	$Rho^{206}Pb/^{238}U$ vs. $^{207}Pb/^{235}U$	f206	^{207}Pb-Corrected Age (Ma)	
	$\times 10^{-6}$	$\times 10^{-6}$		$\times 10^{-6}$									$^{206}Pb\ */^{208}U$ Age	1s
Afan-01	11.8065	67.7355	0.1743	16.4730	0.0877	0.0007	0.4806	0.0071	5.8327	0.1215	0.2549	0.7908	117.3	3.8
Afan-02	4.0775	103.7666	0.0393	45.1296	0.1476	0.0013	0.5213	0.0065	10.6447	0.2100	0.5561	0.8654	126.8	5.9
Afan-03	15.4631	108.6100	0.1424	20.0108	0.0712	0.0006	0.4307	0.0053	4.2467	0.0841	0.5822	0.6994	136.6	2.4
Afan-04	2.0622	93.9476	0.0220	53.5053	0.1883	0.0018	0.5333	0.0063	13.9032	0.2828	0.5992	0.8874	135.3	7.4
Afan-05	5.8139	119.5222	0.0486	25.2833	0.0789	0.0008	0.4517	0.0073	4.9207	0.1078	0.2746	0.7380	131.8	3.5
Afan-06	26.1681	92.0572	0.2843	17.1981	0.0714	0.0006	0.4290	0.0056	4.2362	0.0861	0.4143	0.6963	138.3	2.5
Afan-07	40.3916	49.6936	0.8128	21.0289	0.1426	0.0015	0.5034	0.0062	9.9318	0.2072	0.7708	0.8326	152.1	5.5
Afan-08	2.7450	83.3250	0.0329	47.9422	0.1887	0.0016	0.5250	0.0067	13.6996	0.2738	0.4018	0.8723	153.5	7.8
Afan-09	19.0730	73.8208	0.2584	57.5059	0.2510	0.0023	0.5316	0.0062	18.4598	0.3785	0.7692	0.8843	184.6	9.7
Afan-10	20.5348	38.2165	0.5373	49.5886	0.4293	0.0107	0.5569	0.0066	33.0438	1.0014	0.9273	0.9306	189.2	17.5
Afan-11	0.3130	27.7304	0.0113	21.9052	0.2508	0.0024	0.5507	0.0066	19.0749	0.3698	0.4668	0.9192	129.4	10.2
Afan-12	0.3193	28.4011	0.0112	21.9692	0.2490	0.0024	0.5446	0.0068	18.7374	0.3755	0.5017	0.9080	146.1	10.5
Afan-13	0.1717	19.5985	0.0088	19.2195	0.3103	0.0031	0.5574	0.0072	23.8719	0.4742	0.3877	0.9314	135.7	13.8
Afan-14	7.2094	3.7373	1.9290	37.3037	3.0349	0.0379	0.5941	0.0068	249.2841	5.3132	0.8367	0.9987	25.5	129.8
Afan-15	34.7205	76.5881	0.4533	150.0466	0.6055	0.0054	0.5825	0.0074	48.7498	0.9695	0.4429	0.9775	87.3	27.7
Afan-16	36.1631	83.3387	0.4339	163.3037	0.6053	0.0049	0.5830	0.0073	48.8366	0.9780	0.5286	0.9785	83.5	27.4
Afan-17	32.8148	73.3154	0.4476	133.9739	0.5622	0.0041	0.5853	0.0095	45.5899	1.0326	0.5488	0.9825	63.0	32.2
Afan-18	20.2782	53.6380	0.3781	135.8790	0.7724	0.0059	0.5928	0.0118	63.4210	1.6054	0.5265	0.9963	18.2	54.7
Afan-19	27.6419	62.5068	0.4422	116.3735	0.5756	0.0045	0.5862	0.0169	46.7235	1.5160	0.4744	0.9842	58.5	57.4

Table A2. *Cont.*

Spot	Th	U	Th/U	Pb_{total}	$^{206}Pb/^{238}U$	1s	$^{207}Pb/^{206}Pb$	1s	$^{207}Pb/^{235}U$	1s	$Rho^{206}Pb/^{238}U$ vs. $^{207}Pb/^{235}U$	f206	^{207}Pb-Corrected Age (Ma)	
	$\times 10^{-6}$	$\times 10^{-6}$		$\times 10^{-6}$									^{206}Pb */^{208}U Age	1s
Afan-20	25.7915	59.3968	0.4342	115.0307	0.5931	0.0050	0.5844	0.0197	48.0072	1.7632	0.4857	0.9810	72.2	68.8
Afan-21	26.8284	56.9403	0.4712	101.2443	0.5490	0.0049	0.5752	0.0222	43.7795	1.8089	0.7358	0.9641	125.7	71.3
Afan-22	36.0486	61.2536	0.5885	81.2343	0.4113	0.0032	0.5695	0.0251	32.4847	1.4907	0.5485	0.9536	121.8	60.3
Afan-23	35.0765	58.6545	0.5980	75.3947	0.3958	0.0030	0.5670	0.0279	31.1398	1.5691	0.6236	0.9492	128.4	64.5
Afan-24	34.6682	57.3490	0.6045	69.9870	0.3755	0.0030	0.5625	0.0307	29.2891	1.6090	0.4050	0.9409	141.4	67.3

Note: * denotes radiogenic Pb.

Table A3. Trace element composition of apatite from different localities (μg/g). Reference: * Yang et al. (2014) [50]; ** Zhang et al. (2022) [35]; *** Yuan et al. (2021) [36]; **** Liu and Zhang (2005) [52]; ***** Roda–Robles et al. (2022) [51]. Samples kp03-161 and kp03-308 are from the 1st zone of Altay pegmatites; kp03-401 and kp03-6 are from the 2nd zone; kp03-110 and kp03-309 are from the 3rd zone; kp03-151, kp03-153, and kp03-310 are from the 4th zone; kp03-311 and kp03-407 are from the 5th zone; kp03-314 and kp03-410 are from the 7th zone; and kp03-311 are from the 9th zone. Samples 9-(15) and 10-(15) are barren pegmatites of the Central Iberian zone, 11-(22) and 12-(22) are from P–rich pegmatites, and 13-(15) and 14-(15) are from Li-rich pegmatites. "–" means no available data.

Sample	Sr	Y	La	Ce	Pr	Nd	Sm	Eu	Gd	Tb	Dy	Ho	Er	Tm	Yb	Lu	Th	U	Th/U	$(Ce/Yb)_N$	Eu/Eu *	Ce/Ce *
AP1 *	2506	309	1925	3783	403	1501	205	31	120	14	64	11	25	3	18	2.3	647	24	26.96	58.38	0.56	1.00
AP2 *	591	321	2269	4261	422	1435	178	19	105	12	61	11	26	3.3	20	2.4	2095	66	31.74	59.18	0.39	0.99
Durango Chew *	482	911	4285	5405	488	1677	237	21	204	28	154	32	83	10	59	6	320	20	16.00	25.45	0.28	0.76
Durango Fisher *	456	427	3176	3635	307	1009	127	15	105	13	68	14	34	4	27	4	151	7	21.57	37.40	0.39	0.71
Durango Griffin *	491	886	3819	5178	496	1745	244	22	206	27	146	30	77	10	56	7	270	11	24.55	25.68	0.29	0.79
Durango Hou *	476	762	3334	4561	436	1514	207	20	174	23	123	25	64	8	47	6	231	11	21.00	26.96	0.31	0.80
MAD *	1650	257	1745	3338	349	1290	173	25	102	12	53	9.2	21	2.4	15	1.9	661	19	34.79	61.81	0.53	0.99
Otter Lake *	1668	889	2772	6832	832	3205	445	78	275	34	173	33	85	11	68	8.4	753	99	7.61	27.91	0.63	1.09
NW-1 *	5512	851	3576	7477	865	3468	582	169	400	49	225	34	68	7	35	3.6	48	122	0.39	59.34	1.01	1.01
Slyudyanka *	1231	46	77	140	14	53	10	2	9	1	8	2	5	1	4	0.48	142	68	2.09	9.72	0.63	0.97
UWA-1 *	1186	3583	2857	6876	901	3747	731	93	676	114	716	154	421	55	311	31	828	165	5.02	6.14	0.40	1.04
Mud Tank *	2681	73	414	980	237	550	93	25	64	6.4	25	3.4	6	0.5	2.4	0.25	11	2.1	5.24	113.43	0.94	0.76

Table A3. *Cont.*

Sample	Sr	Y	La	Ce	Pr	Nd	Sm	Eu	Gd	Tb	Dy	Ho	Er	Tm	Yb	Lu	Th	U	Th/U	$(Ce/Yb)_N$	Eu/Eu *	Ce/Ce *
McClure Mountain *	3422	206	1609	2362	126	843	102	37	77	8.3	40	7.4	18	2.3	14	1.9	38	12	3.17	46.87	1.23	0.95
SDG *	11,368	605	7209	15,668	1843	7344	911	196	468	38	140	21	49	5.5	33	4.3	705	47	15	131.89	0.82	1.03
MADB **	3093.09	–	2231.74	4651.92	447.2	1769.42	254.67	39.2	163.59	17.93	83.52	14.29	33.09	3.79	21.68	2.92	–	–	–	59.60	0.55	1.08
Moro ***	618.13	–	2117.01	2763.91	193.71	639.77	90.72	14.78	77.45	9.68	55.94	10.67	28.34	3.78	22.79	2.99	–	184.37	–	33.69	0.53	0.82
kp03-161 ****	308.57	114.91	72.83	119.64	10.27	25.67	8.95	2.77	7.07	2.37	13.72	1.99	6.19	1.55	15.53	2.17	–	–	–	2.14	1.07	0.94
kp03-308 ****	11.23	672.94	395.14	1057.11	115.86	315.98	140.93	1.51	114.37	34.23	141.3	11.57	19.72	2.42	14.09	1.26	–	–	–	20.84	0.04	1.20
kp03-401 ****	14.59	528.54	390.66	1028.5	108.58	272.65	127.51	1.68	95.33	25.55	118.17	11.02	18.17	2.52	15.02	1.42	–	–	–	19.02	0.05	1.20
kp03-6 ****	6.46	185.72	333.39	562	41.47	71.8	20.74	0.39	13.8	4.81	24.13	2.39	5.52	1.06	7.99	0.83	–	–	–	19.54	0.07	1.00
kp03-71 ****	11.62	172.99	368.32	555.65	38.53	61.89	16.8	0.25	12.54	4.38	21.71	2.16	4.99	0.94	6.9	0.7	–	–	–	22.37	0.05	0.93
kp03-104 ****	8.15	203.98	404.07	626.27	45.15	73.11	20.74	0.35	14.26	5.08	25.66	2.52	6.01	1.09	9	0.87	–	–	–	19.33	0.06	0.94
kp03-110 ****	11.65	34.23	177.96	137.65	6.75	14.12	4.08	0.33	3.42	1.02	4.82	0.46	0.95	0.15	1.05	0.09	–	–	–	36.42	0.26	0.55
kp03-309 ****	13.45	599.97	440.86	1041.06	99.5	242.59	94.8	1.22	71.91	23.01	100.73	9	18.17	2.81	17.96	1.78	–	–	–	16.10	0.05	1.17
kp03-151 ****	42.49	3.87	4.27	5.73	0.32	0.39	0.21	0	0.22	0.1	0.51	0.05	0.1	0.03	0.2	0.02	–	–	–	7.96	0.06	0.88
kp03-153 ****	10.53	113.77	361.81	373.79	28.07	43.62	11.91	0.32	9.53	2.98	13.88	1.35	2.99	0.55	3.93	0.35	–	–	–	26.42	0.09	0.67
kp03-310 ****	14.23	25.44	116.9	92.07	4.91	8.64	3.42	0.21	2.82	0.83	3.86	0.41	0.74	0.12	0.72	0.08	–	–	–	35.52	0.21	0.55
kp03-311 ****	284.56	403	173	299.37	26.47	67.84	26.91	1.15	24.18	8.6	51.18	7.53	23.73	5.46	51.62	6.77	–	–	–	1.61	0.14	0.97
kp03-407 ****	260.23	335.63	166.65	286.46	25.14	60.29	25.9	1.04	21.76	6.91	45.11	7.38	23.57	5.53	53.31	7.2	–	–	–	1.49	0.13	0.97
kp03-312 ****	317.14	144.79	88.31	133.87	10.44	24.55	8.12	0.54	7.65	2.66	15.74	2.33	8.19	2.07	22.15	3.19	–	–	–	1.68	0.21	0.91
kp03-313 ****	297.39	238.7	118.49	191.04	15.71	37.2	13.83	0.85	12.51	4.32	26.82	3.99	12.66	3.22	32.82	4.46	–	–	–	1.62	0.19	0.94
kp03-314 ****	61.93	52.81	46.46	62.46	4.43	10.03	4.02	0.23	3.63	1.28	6.63	0.8	2.29	0.5	4.43	0.55	–	–	–	3.92	0.18	0.84
kp03-410 ****	9.94	4.5	5.55	10.28	0.98	2.79	0.83	0.02	0.69	0.19	0.89	0.08	0.18	0.03	0.16	0.02	–	–	–	17.85	0.09	1.00
kp03-318 ****	265.17	211.44	132.7	197.29	14.81	31.5	12.26	0.52	9.89	3.84	21.53	2.95	9.33	2.25	24.34	3.36	–	–	–	2.25	0.14	0.90
9-(15) *****	136	599	249	472	50	158	44	5	46	11	76	14	46	9	75	10	5	187	0.03	1.75	0.34	0.98
10-(15) *****	733	456	201	399	38	125	33	6	34	8	55	11	36	7	57	8	2	229	0.01	1.94	0.54	1.04
11-(22) *****	66.9	940	33	230	63.9	382	319	4.9	432	94.2	436	42	70	7.3	34.9	2.8	1.2	67	0.02	1.83	0.04	0.93
12-(22) *****	217	577	540	1740	271	1050	405	6.5	289	48.9	211	19.2	33.7	4	22.4	2.2	26.5	272	0.01	21.58	0.06	1.11
13-(15) *****	7610	24	26	42	4	13	2	8	1	0	2	0	1	0	3	0	22	3	7.33	3.89	15.38	0.90
14-(14) *****	4366	134	56	171	21	87	19	8	18	3	19	4	12	2	11	1	13	1	13	4.32	1.30	1.22

References

1. Belousova, E.A.; Griffin, W.L.; O'Reilly, S.Y.; Fisher, N.I. Apatite as an Indicator Mineral for Mineral Exploration: Trace-Element Compositions and Their Relationship to Host Rock Type. *J. Geochem. Explor.* **2002**, *76*, 45–69. [CrossRef]
2. Bruand, E.; Fowler, M.; Storey, C.; Darling, J. Apatite Trace Element and Isotope Applications to Petrogenesis and Provenance. *Am. Mineral.* **2017**, *102*, 75–84. [CrossRef]
3. Hu, S.; Lin, Y.; Zhang, J.; Hao, J.; Xing, W.; Zhang, T.; Yang, W.; Changela, H. Ancient Geologic Events on Mars Revealed by Zircons and Apatites from the Martian Regolith Breccia NWA 7034. *Meteorit. Planet. Sci.* **2019**, *54*, 850–879. [CrossRef]
4. Boyce, J.W.; Liu, Y.; Rossman, G.R.; Guan, Y.; Eiler, J.M.; Stolper, E.M.; Taylor, L.A. Lunar Apatite with Terrestrial Volatile Abundances. *Nature* **2010**, *466*, 466–469. [CrossRef] [PubMed]
5. Gross, J.; Filiberto, J.; Herd, C.D.K.; Daswani, M.M.; Schwenzer, S.P.; Treiman, A.H. Petrography, Mineral Chemistry, and Crystallization History of Olivine-Phyric Shergottite NWA 6234: A New Melt Composition. *Meteorit. Planet. Sci.* **2013**, *48*, 854–871. [CrossRef]
6. McCubbin, F.M.; Hauri, E.H.; Elardo, S.M.; Vander Kaaden, K.E.; Wang, J.; Shearer, C.K. Hydrous Melting of the Martian Mantle Produced Both Depleted and Enriched Shergottites. *Geology* **2012**, *40*, 683–686. [CrossRef]
7. Patiño Douce, A.E.; Roden, M.F.; Chaumba, J.; Fleisher, C.; Yogodzinski, G. Compositional Variability of Terrestrial Mantle Apatites, Thermodynamic Modeling of Apatite Volatile Contents, and the Halogen and Water Budgets of Planetary Mantles. *Chem. Geol.* **2011**, *288*, 14–31. [CrossRef]
8. Xu, B.; Hou, Z.-Q.; Griffin, W.L.; Yu, J.-X.; Long, T.; Zhao, Y.; Wang, T.; Fu, B.; Belousova, E.; O'Reilly, S.Y. Apatite Halogens and Sr-O and Zircon Hf-O Isotopes: Recycled Volatiles in Jurassic Porphyry Ore Systems in Southern Tibet. *Chem. Geol.* **2022**, *16*, 120924. [CrossRef]
9. Xu, B.; Hou, Z.-Q.; Griffin, B.; Lu, Y.; Belousova, E.; Xu, J.-F.; O'Reilly, S.Y. Recycled Volatiles Determine Fertility of Porphyry Deposits in Collisional Settings. *Am. Mineral.* **2021**, *106*, 656–661. [CrossRef]
10. Xu, B.; Hou, Z.Q.; Griffin, W.L.; O'Reilly, S.Y.; Zheng, Y.C.; Wang, T.; Xu, J.F. In-Situ Mineralogical Interpretation of the Mantle Geophysical Signature of the Gangdese Cu-Porphyry Mineral System. *Gondwana Res.* **2022**, *111*, 53–63. [CrossRef]
11. Xu, B.; Griffin, W.L.; Xiong, Q.; Hou, Z.-Q.; O'Reilly, S.Y.; Guo, Z.; Pearson, N.J.; Gréau, Y.; Yang, Z.-M.; Zheng, Y.-C. Ultrapotassic Rocks and Xenoliths from South Tibet: Contrasting Styles of Interaction between Lithospheric Mantle and Asthenosphere during Continental Collision. *Geology* **2017**, *45*, 51–54. [CrossRef]
12. YingXiong, B.; Ping, S.; Chong, C.; HongDi, P.; ChangHao, L.; YaoQing, L.; HaoXuan, F.; QingYu, S. Geochemical Charac-teristics and Significance of Apatite from the Koktokay Pegmatitic Rare-Metal Deposit, Altay, Xinjiang. *Acta Petrol. Sin.* **2021**, *37*, 2843–2860. [CrossRef]
13. Miles, A.J.; Graham, C.M.; Hawkesworth, C.J.; Gillespie, M.R.; Hinton, R.W.; Bromiley, G.D. Apatite: A New Redox Proxy for Silicic Magmas? *Geochim. Cosmochim. Acta* **2014**, *132*, 101–119. [CrossRef]
14. Stokes, T.N.; Bromiley, G.D.; Potts, N.J.; Saunders, K.E.; Miles, A.J. The Effect of Melt Composition and Oxygen Fugacity on Manganese Partitioning between Apatite and Silicate Melt. *Chem. Geol.* **2019**, *506*, 162–174. [CrossRef]
15. Bromiley, G.D. Do Concentrations of Mn, Eu and Ce in Apatite Reliably Record Oxygen Fugacity in Magmas? *Lithos* **2021**, *384–385*, 105900. [CrossRef]
16. Zafar, T.; Leng, C.-B.; Zhang, X.-C.; Rehman, H.U. Geochemical Attributes of Magmatic Apatite in the Kukaazi Granite from Western Kunlun Orogenic Belt, NW China: Implications for Granite Petrogenesis and Pb-Zn (-Cu-W) Mineralization. *J. Geochem. Explor.* **2019**, *204*, 256–269. [CrossRef]
17. Zhu, J.; Wu, C.; Liu, C.; Li, F.; Huang, X.; Zhou, D. Magmatic—Hydrothermal Evolution and Genesis of Keketouhai No·3 Rare Metal Pegmatite Dyke, Altai, China. *Geol. J. China Univ.* **2000**, *6*, 40–52. [CrossRef]
18. Wu, C.; Zhu, J.; Liu, C.; Yang, S.; Zhu, B.; Ning, G. A Study on thr Inclusions in Spodumenes. *Geotecton. Metallog.* **1994**, *18*, 353–362.
19. Zheng, F.; Wang, G.; Ni, P. Research progress on the fluid metallogenic mechanism of granitic pegmatite-type rare metal deposits. *J. Geomech.* **2021**, *27*, 596–613. [CrossRef]
20. London, D. Ore-Forming Processes within Granitic Pegmatites. *Ore Geol. Rev.* **2018**, *101*, 349–383. [CrossRef]
21. Chew, D.M.; Spikings, R.A. Apatite U–Pb Thermochronology: A Review. *Minerals* **2021**, *11*, 1095. [CrossRef]
22. Lyckberg, P. Afghan Pegmatites. *Mineral. Record.* **2017**, *48*, 610–675.
23. Cocker, M. Summaries of Important Areas for Mineral Investment and Production Opportunities of Nonfuel Minerals in Afghanistan. In *Summaries of Important Areas for Mineral Investment and Production Opportunities of Nonfuel Minerals in Afghanistan*; U.S. Geological Survey: Tacoma, WA, USA, 2011.
24. Ahmadi, H.M.; Yousufi, A. *The Zoning Structure of The Rare—Metal Pegmatites of Afghanistan*; Iran Geological Survey: Tehran, Iran, 2018.
25. Kufner, S.-K.; Kakar, N.; Bezada, M.; Bloch, W.; Metzger, S.; Yuan, X.; Mechie, J.; Ratschbacher, L.; Murodkulov, S.; Deng, Z.; et al. The Hindu Kush Slab Break-off as Revealed by Deep Structure and Crustal Deformation. *Nat Commun.* **2021**, *12*, 1685. [CrossRef] [PubMed]
26. Waizy, H.; Moles, N.R.; Smith, M.P.; Boyce, A.J. Formation of the Giant Aynak Copper Deposit, Afghanistan: Evidence from Mineralogy, Lithogeochemistry and Sulphur Isotopes. *Int. Geol. Rev.* **2021**, *63*, 2104–2128. [CrossRef]

27. Xiang, D.; Zhang, Z.; Zack, T.; Chew, D.; Yang, Y.; Wu, L.; Hogmalm, J. Apatite U–Pb Dating with Common Pb Correction Using LA-ICP-MS/MS. *Geostand. Geoanalytical Res.* **2021**, *45*, 621–642. [CrossRef]
28. Thomson, S.N.; Gehrels, G.E.; Ruiz, J.; Buchwaldt, R. Routine Low-Damage Apatite U–Pb Dating Using Laser Ablation–Multicollector–ICPMS. *Geochem. Geophys. Geosystems* **2012**, *13*. [CrossRef]
29. Chew, D.M.; Petrus, J.A.; Kamber, B.S. U–Pb LA–ICPMS Dating Using Accessory Mineral Standards with Variable Common Pb. *Chem. Geol.* **2014**, *363*, 185–199. [CrossRef]
30. Ludwig, K.R. *User's Manual for Isoplot Version 3.75e4.15: A Geochronological Toolkit for Microsoft Excel*; Berkeley Geochronological Center Special Publication: Berkeley, CA, USA, 2012.
31. Ross, S.D. Phosphates and Other Oxy-Anions of Group V. In *The Infrared Spectra of Minerals*; Farmer, V.C., Ed.; Mineralogical Society of Great Britain and Ireland: Londan, UK, 1974; Volume 4.
32. Blakeslee, K.C.; Condrate, R.A., Sr. Vibrational Spectra of Hydrothermally Prepared Hydroxyapatites. *J. Am. Ceram. Soc.* **1971**, *54*, 559–563. [CrossRef]
33. Antonakos, A.; Liarokapis, E.; Leventouri, T. Micro-Raman and FTIR Studies of Synthetic and Natural Apatites. *Biomaterials* **2007**, *28*, 3043–3054. [CrossRef]
34. Hammerli, J.; Hermann, J.; Tollan, P.; Naab, F. Measuring in Situ CO_2 and H_2O in Apatite via ATR-FTIR. *Contrib Miner. Petrol.* **2021**, *176*, 105. [CrossRef]
35. Zhang, Z.-Y.; Xu, B.; Yuan, P.-Y.; Wang, Z.-X. Gemological and Mineralogical Studies of Greenish Blue Apatite in Madagascar. *Crystals* **2022**, *12*, 1067. [CrossRef]
36. Yuan, P.; Xu, B.; Wang, Z.; Liu, D. A Study on Apatite from Mesozoic Alkaline Intrusive Complexes, Central High Atlas, Morocco. *Crystals* **2022**, *21*, 461. [CrossRef]
37. Penel, G.; Leroy, G.; Rey, C.; Sombret, B.; Huvenne, J.P.; Bres, E. Infrared and Raman Microspectrometry Study of Fluor-Fluor-Hydroxy and Hydroxy-Apatite Powders. *J. Mater. Sci. Mater. Med.* **1997**, *8*, 271–276. [CrossRef]
38. Penel, G.; Leroy, G.; Rey, C.; Bres, E. MicroRaman Spectral Study of the PO4 and CO3 Vibrational Modes in Synthetic and Biological Apatites. *Calcif. Tissue Int.* **1998**, *63*, 475–481. [CrossRef] [PubMed]
39. Cuscó, R.; Guitián, F.; de Aza, S.; Artús, L. Differentiation between Hydroxyapatite and β-Tricalcium Phosphate by Means of μ-Raman Spectroscopy. *J. Eur. Ceram. Soc.* **1998**, *18*, 1301–1305. [CrossRef]
40. Zhukova, I.A.; Stepanov, A.S.; Korsakov, A.V.; Jiang, S.-Y. Application of Raman Spectroscopy for the Identification of Phosphate Minerals from REE Supergene Deposit. *J. Raman Spectrosc.* **2022**, *53*, 485–496. [CrossRef]
41. Pieczka, A.; Gołębiowska, B.; Jeleń, P.; Sitarz, M.; Szuszkiewicz, A. Raman Spectroscopic Studies of O–H Stretching Vibration in Mn-Rich Apatites: A Structural Approach. *Am. Mineral.* **2020**, *105*, 1385–1391. [CrossRef]
42. Penel, G.; Cau, E.; Delfosse, C.; Rey, C.; Hardouin, P.; Jeanfils, J.; Delecourt, C.; Lemaitre, J.; Leroy, G. Raman Microspectrometry Studies of Calcified Tissues and Related Biomaterials. Raman Studies of Calcium Phosphate Biomaterials. *Dent. Med. Probl.* **2003**, *40*, 37–43.
43. Mészárosová, N.; Skála, R.; Matoušková, Š.; Mikysek, P.; Plášil, J.; Císařová, I. Hydrothermal-to-Metasomatic Overprint of the Neovolcanic Rocks Evidenced by Composite Apatite Crystals: A Case Study from the Maglovec Hill, Slanské Vrchy Mountains, Slovakia. *Geol. Carpathica* **2018**, *69*, 439–452. [CrossRef]
44. Chakhmouradian, A.R.; Reguir, E.P.; Zaitsev, A.N.; Couëslan, C.; Xu, C.; Kynický, J.; Mumin, A.H.; Yang, P. Apatite in Carbonatitic Rocks: Compositional Variation, Zoning, Element Partitioning and Petrogenetic Significance. *Lithos* **2017**, *274–275*, 188–213. [CrossRef]
45. Liu, Y. Mineralogical Spectroscopy of Apatites. Ph.D. Thesis, Sun Yai-Sen University, Guangzhou, China, 2003.
46. Sun, S.-s.; McDonough, W.F. Chemical and Isotopic Systematics of Oceanic Basalts: Implications for Mantle Composition and Processes. In *Geological Society*; Special Publications: London, UK, 1989; Volume 42, pp. 313–345. [CrossRef]
47. Young, E.J. Mineralogy and Geochemistry of Fluorapatite from Cerro de Mercado, Durango, Mexico. *USGS Prof. Pap.* **1969**, *650*, D85–D92.
48. Zolotarev, V.M. Optical Constants of an Apatite Single Crystal in the IR Range of 6–28 Mm. *Opt. Spectrosc.* **2018**, *124*, 262–272. [CrossRef]
49. Ulian, G. Ab Initio Quantum Mechanical Investigation of Structural and Chemical-Physical Properties of Selected Minerals for Minero-Petrological, Structural Ceramic and Biomaterial Applications. Ph.D. Thesis, Alma Mater Studiorum Università di Bologna, Bologna, Italy, 2014. [CrossRef]
50. Yang, Y.-H.; Wu, F.-Y.; Yang, J.-H.; Chew, D.M.; Xie, L.-W.; Chu, Z.-Y.; Zhang, Y.-B.; Huang, C. Sr and Nd Isotopic Compositions of Apatite Reference Materials Used in U–Th–Pb Geochronology. *Chem. Geol.* **2014**, *385*, 35–55. [CrossRef]
51. Roda-Robles, E.; Gil-Crespo, P.P.; Pesquera, A.; Lima, A.; Garate-Olave, I.; Merino-Martínez, E.; Cardoso-Fernandes, J.; Errandonea-Martin, J. Compositional Variations in Apatite and Petrogenetic Significance: Examples from Peraluminous Granites and Related Pegmatites and Hydrothermal Veins from the Central Iberian Zone (Spain and Portugal). *Minerals* **2022**, *12*, 1401. [CrossRef]
52. Liu, C.-Q.; Zhang, H. The Lanthanide Tetrad Effect in Apatite from the Altay No. 3 Pegmatite, Xingjiang, China: An Intrinsic Feature of the Pegmatite Magma. *Chem. Geol.* **2005**, *214*, 61–77. [CrossRef]
53. Cao, M.-J.; Zhou, Q.-F.; Qin, K.-Z.; Tang, D.-M.; Evans, N.J. The Tetrad Effect and Geochemistry of Apatite from the Altay Koktokay No. 3 Pegmatite, Xinjiang, China: Implications for Pegmatite Petrogenesis. *Min. Petrol.* **2013**, *107*, 985–1005. [CrossRef]

54. Li, J.; Chen, S.-Y.; Zhao, Y.-H. Trace Elements in Apatite from Gejiu Sn Polymetallic District: Implications for Petrogenesis, Metallogenesis and Exploration. *Ore Geol. Rev.* **2022**, *145*, 104880. [CrossRef]
55. Bau, M. Controls on the Fractionation of Isovalent Trace Elements in Magmatic and Aqueous Systems: Evidence from Y/Ho, Zr/Hf, and Lanthanide Tetrad Effect. *Contrib Miner. Petrol.* **1996**, *123*, 323–333. [CrossRef]

Disclaimer/Publisher's Note: The statements, opinions and data contained in all publications are solely those of the individual author(s) and contributor(s) and not of MDPI and/or the editor(s). MDPI and/or the editor(s) disclaim responsibility for any injury to people or property resulting from any ideas, methods, instructions or products referred to in the content.